Versatile and Rapid Synthesis of Polymer Nanodomes via Template- and Solvent-Free Condensed Droplet Polymerization

*Trevor Franklin, Danielle L. Streever, Rong Yang**

Robert Frederick Smith School of Chemical & Biomolecular Engineering, Cornell University, 120 Olin Hall, Ithaca, NY 14853, United States

Abstract: Non-spherical polymer nanoparticles (PNPs) represent an emerging class of materials with novel functions such as self-assembly of metamaterials and programmable pharmacokinetics/immune response. Common solution-based synthesis techniques like emulsion polymerization primarily produce spherical particles. Although non-spherical PNPs have been obtained with additional templating, fabrication, and purification steps, the labor-intensive and costly solution-based synthetic protocols limit the fundamental and applied research on their properties and functions. Furthermore, these approaches are only applicable to a small selection of monomers, restricting the functionality that is accessible by PNPs. Here we report the rapid, solvent- and template-free synthesis of non-spherical PNPs via the fresh idea of coupled condensation and polymerization, realized using a novel technique, namely condensed droplet polymerization (CDP). Using polymer nanodomes as a proof-of-principle, we demonstrate continuous variation of particle dimensions (from sub-20 nm to above 1 μm) and the complete syntheses of nanodomes comprised of a variety of functional polymers within seconds to minutes. The vapor-based CDP approach renders the technique scalable for the manufacturing of soft non-spherical nanoparticles, promising to advance applications

1. Introduction

The shape of polymer nanoparticles (PNPs) has profound impact on their utility, and the development of non-spherical PNPs is key to both advancements in the fundamental understanding of emergent properties (e.g., in the self-assembly and jamming of particles) and discovery of new materials and functions. Suspensions of shape-controlled nanoparticles have demonstrated rheological properties necessary for impact-resistance or improvement of paint and printing products [1,2]. Engineering the shape of PNPs studied for drug delivery has also shown to influence biodistribution, circulation time, and controlled release of a payload, to improve targeting efficiency, and to reduce side effects faced by spherical particles in both systemic and local delivery (e.g., to enhance the aerodynamics for improved efficacy of inhaled powder drugs) [2–5]. Nevertheless, non-spherical PNPs have only been achieved via sophisticated multistep syntheses and fabrication procedures, throttling the discovery of a richer palette of soft nanomaterials and novel emergent functions while prohibiting their manufacturing at scale [4,6,7]. In particular, dome-shaped or hemispherical polymer nanoparticles, despite their revolutionizing potential as nano-lenses for super-resolution microscopy and enabling theranostic materials [8], have been obtained by the elaborate procedures of synthesizing and subsequently cleaving Janus particles [9,10]. Such highly specialized synthesis procedures represent a critical challenge in enabling the broader investigation and application of shape-controlled PNPs, leaving their functional potentials underexplored.

To realize the facile and scalable synthesis of nanoparticles with diverse morphologies and geometries, research on inorganic particles has employed the solvent-free chemical vapor deposition (CVD) technique, a foundational technology across manufacturing industries ranging from consumer goods to advanced electronics, where delivery of reactants are precisely controlled

to yield targeted particle shapes and dimensions [11–13], However, CVD techniques have not been broadly translated to polymeric particles. While CVD-based polymerization techniques are often used to produce polymer thin films on a substrate, if successfully adapted for the synthesis of polymer particles, their solvent-free characteristic would overcome many limitations of conventional solution-based PNP synthesis procedures.

The most common bottom-up PNP synthesis method is emulsion polymerization in which a monomer with low water solubility is introduced to water along with a water-soluble initiator and surfactant(s) [14–16]. Other bottom-up synthetic techniques include membrane emulsification in which step polymerization occurs at the interface of two liquid phases in which two reactive monomers are dissolved [17]. These conventional PNP synthesis approaches share the same fundamental mechanism for PNP formation, i.e., PNPs emerge at phase boundaries driven by minimization of interfacial free energy, leading to the predominance of the spherical particle shape in existing studies. The use of solvents also presents a number of additional drawbacks. The chemical functionalities of PNPs resulting from solution-based protocols are primarily limited to those afforded by the monomers that are soluble or can be emulsified. Inclusion of solvents or surfactants, which are often toxic, requires costly additional removal steps for a purified product (e.g., for nanomedicine). Furthermore, the need for purification elongates the already time-consuming synthetic protocols for PNPs that could take up to several days [18]. A synthetic approach that introduces only reactants (i.e., a solution-free system) and achieves complete polymerization, like that of CVD for thin films, would evade the requirement of purification steps and remove the restrictions on particle shapes and chemical functionalities, enabling rapid and scalable synthesis of PNPs with high purity in one step.

We report here a new technique named condensed droplet polymerization (CDP) that utilizes free radical polymerization, similar to that performed in initiated chemical vapor deposition (iCVD), to synthesize solid polymer nanodomes from vapor phase reagents. While vapor deposition has been used to synthesize inorganic nanoparticles and to modify or encapsulate nanoparticles synthesized by conventional methods, the template- and solvent-free synthesis of PNPs has not been achieved [19,20]. Prior CVD-based syntheses of polymer particles required solvents (e.g., ionic liquids) and/or templates (e.g., sublimating solids or structured liquids), which nevertheless limited the particles to a spherical shape and a small selection of chemical functionalities [21–24]. Using CDP, we polymerized nanodomes bearing a diverse range of functionalities in less than 45 seconds. The CDP protocol is composed of two steps that are expanded upon in Section 3.1: (i) condensation, controlled at the nanoscale; and (ii) droplet polymerization, by impinging free radical initiators formed in the vapor phase. The resulting polymer nanodomes could find novel applications in soft robotics, injectable implants, drug delivery and theranostics in medicine [7], agriculture (e.g., plant growth regulation) [25], and consumer goods (e.g., nutrient enhancement in food preparation) [26].

2. Experimental Section

2.1 Base Layer Application to Substrate

All purchased chemicals were used as received without modification. Silicon (Si) wafers (Pure Wafer) coated with fluorinated thin films were prepared using the initiated chemical vapor deposition (iCVD) technique in a custom built reactor comprised of parts and dimensions detailed in a previous publication [27]. A silicon wafer was placed in the iCVD reactor chamber held at 400

mTorr on a temperature-controlled stage maintained at 35 °C. A glass jar containing 1H,1H,2H,2H-perfluorofecyl acrylate (PFDA, Sigma-Aldrich, 97%) was heated to 80 °C and the monomer vapors were delivered to the vacuum chamber through a needle valve at flow rate of 0.15 sccm. Argon carrier gas and tert-butyl peroxide (TBPO) were also delivered into the chamber through mass flow controllers at 2.00 sccm and 0.60 sccm respectively. A filament array composed of 0.5 mm copper/nickel wire (55% Cu/45% Ni, Goodfellow) was positioned 3 cm above the substrate stage and heated to 300 °C to thermally decompose TPBO into *tert*-butoxyl and methyl radicals. Contact of radicals with PFDA molecules adsorbed to the Si wafer initiated the thin film polymerization. The deposition thickness was observed in real time using an interferometer with a 633 nm helium-neon laser (JDS Uniphase) until a coating between 100 and 200 nm was formed (approximated due to significant surface roughness).

Poly(PFDA) (PPFDA) thin films can exhibit rough surfaces due to randomly-oriented crystalline domains caused by alignment of the fluorinated side chains (Figure S1) [28]. To ensure a flat layer for the condensed droplet polymerization (CDP), PPFDA films were placed in an oven set to 80 °C for one hour. At this temperature, roughness on the order of hundreds of nanometers is reduced to picometer range by eliminating organized crystalline domains responsible for surface protrusions [29].

A poly(1*H*,1*H*,2*H*,2*H*-perfluorooctyl acrylate) (PPFOA, SynQuest Laboratories, 97%) base layer was prepared according to the same procedure with PFOA as a monomer and using the following conditions: PFOA, TBPO, and argon flow rates of 0.2, 0.6, and 1.0 sccm, respectively; reactor chamber pressure of 400 mTorr; filament array temperature of approximately 270 °C; stage temperature of 30 °C. A P4VP base layer was prepared according to the same procedure with 4VP as a monomer and the following conditions: 4VP, TBPO, and argon flow rates of 4.1, 0.5, and 0.8

sccm, respectively; reactor chamber pressure of 400 mTorr; filament array temperature of approximately 270 °C; stage temperature of 25 °C. A PHEMA base layer was prepared according the same procedure with HEMA as a monomer and the following conditions: HEMA, TBPO, and argon flow rates of 0.2, 0.3, and 0.3 sccm, respectively; reactor chamber pressure of 300 mTorr; filament array temperature of approximately 270 °C; stage temperature of 30 °C.

2.2 Nanodome synthesis via CDP

Silicon wafer substrates with fluorinated base layers were placed into the iCVD reactor atop a thermoelectric cooling device (TEC, VT-127-1.0-1.3-71, TE Technology). A ceramic thermal compound (Céramique^{TM} 2, Arctic Silver) was used to secure the TEC to underlying stage that was held at 15-20 °C stage and the reactor chamber was evacuated to below 5 mTorr. The TEC was cooled to below 10 °C by the application of electrical current from a DC power source (1715A, B&K Precision) and the filament array was heated to approximately 300 °C using another DC power source of the same type. A throttle valve (253B, MKS Instruments) was then closed at the outlet to the vacuum pump to isolate the reactor chamber containing the substrate. Liquid monomer stock was heated in a glass jar to generate vapors that were metered into the reactor through a needle valve [HEMA (Sigma-Aldrich, >99%) was heated to 80 °C, 4VP (Sigma-Aldrich, 95%) was heated to 50 °C, and DVB (Sigma-Aldrich, 80%) was heated to 65 °C, glycidyl methacrylate (Sigma-Aldrich, 97%) was heated to 70 °C, benzyl methacrylate (Sigma-Aldrich, 96%) was heated to 75 °C, cyclohexyl methacrylate (Sigma-Aldrich, ≥97%) was heated to 75 °C, 2-(dimethylamino)ethyl methacrylate (Sigma-Aldrich, 98%) was heated to 50 °C, 1-vinylimidazole (Thermo Scientific, 99%) was heated to 75 °C, ethylene glycol dimethacrylate

(Acros, 98%) was heated to 80 °C,]. Influx of monomer vapor increased the pressure until the saturation pressure (monomer-dependent; typically between 10-150 mTorr) was reached and condensation formed on the base layer. Droplet formation was monitored with two in-situ devices: the aforementioned laser interferometer and a digital microscope (VHX 970F, Keyence). The interferometer signal dropped precipitously due to the scattering of the laser aimed at the reflective substrate by the condensed droplets. Simultaneously, the digital microscope showed the droplets as they formed. Once proper droplet size was achieved, monomer flow was stopped. TBPO was delivered to the chamber at 1.80 sccm for 15-45 seconds to initiate polymerization. After TBPO flow stopped, the contents of the chamber were allowed to continue polymerizing at a stable pressure for an additional 15 seconds. Finally, the throttle valve at the outlet to the vacuum pump was opened to stop the reaction and clear the chamber of all vapors and unreacted monomer.

2.3 Characterization of polymer nanodome chemistry

FTIR spectra of polymer films and nanodomes on Si wafers were collected using a Bruker VERTEX Series V80v spectrometer in transmission mode and a mercury cadmium telluride (MCT) detector. Spectra recorded across a range of 4000-600 cm^{-1} (4 cm^{-1} resolution) were averaged over 128 scans, background corrected using a bare Si wafer, and baseline corrected. A P4VP thin film was prepared for FTIR analysis according the iCVD procedure detailed in Subsection 2.1 with 4VP as a monomer and the following conditions: 4VP, TBPO, and argon flow rates of 3.7, 0.5, and 1.0 sccm, respectively; reactor chamber pressure of 400 mTorr; filament array temperature of approximately 250 °C; stage temperature of 25 °C. A PDVB thin film was prepared for FTIR analysis according to the same procedure with DVB as a monomer and the following

conditions: DVB, TBPO, and argon flow rates of 0.6, 0.5, and 0.8 sccm, respectively; reactor chamber pressure of 400 mTorr; filament array temperature of approximately 250 °C; stage temperature of 15 °C. A PHEMA thin film was prepared according the same procedure with HEMA as a monomer and the following conditions: HEMA, TBPO, and argon flow rates of 0.5, 0.9, and 1.3 sccm, respectively; reactor chamber pressure of 300 mTorr; filament array temperature of approximately 270 °C; stage temperature of 30 °C.

SEM and EDX were performed on a Zeiss GeminiSEM 500 on samples that had been coated with approximately 3 nm of gold/palladium. Acceleration voltages used were 1 kV for SEM images and 3 kV for EDX element mapping.

For MALDI-TOF, 3 CDP syntheses of ndHEMA particles were performed according to the above procedure detailed in Subsection 2.2. The polymer content (npHEMA domes and PPFDA base layer) was scraped off of each Si wafer substrate using a clean razor blade into a microcentrifuge tube into which methanol (100 μL) was added to dissolve only the ndHEMA nanodomes. The PHEMA thin film (approximately 3 mg) synthesized according to the protocol above was scraped off of the Si wafer substrate into a microcentrifuge tube into which methanol (100 μL) was added to dissolve the film. A stock matrix solution was prepared by dissolving α-cyano-4-hydroxycinnamic acid (20 μg, CHCA, Sigma-Aldrich, >98%) in methanol (1 mL). The polymer-containing solutions were mixed with the matrix solution and purified water in a ratio of 1:1:0.4 (polymer solution:matrix solution:water), vortexed, spotted onto the MALDI-TOF analysis plate, and allowed to dry completely. MALDI-TOF spectra were collected using a Bruker autoflex maX in positive reflectron mode, smoothed and baseline subtracted, and analyzed using Polymerix (Sierra Analytics). In Polymerix, homopolymer analysis was performed to match the m/z values of the predominant (most intense) peak series by alteration of the alpha and omega end groups.

Analysis was performed up to m/z = 6000, at which point peaks were indistinguishable from the background noise.

Raman spectra were collected of polymer domes over 1 μm in diameter on Si wafers using a WITec alpha300 R Raman imaging microscope. All spectra were recorded using a 523 nm laser, a power of approximately 0.45 mW, a 100x objective. Spectra were recorded with a spectral resolution of 3 cm^{-1} using 300 lines/mm and an accumulation of 10 scans of 10 seconds each.

2.4 npHEMA nanodome diameter dispersity

Dispersity analysis was performed using FIJI. Ten top-down SEM images were recorded across a substrate containing ndHEMA nanodomes synthesized according to the above procedure. FIJI was used to identify the circular cross section of the nanodomes and filter out nanodomes smaller than 8 nm in diameter to avoid detection of blemishes on the substrate layer. Feret's diameter of 416 particles were plotted in a histogram.

2.5 Contact angle and aspect ratio analysis

Contact angle measurements were performed using a Ramé-Hart Model 500 contact angle goniometer. A pipette was used to dispense 5 μL of liquid HEMA, 4VP, and DVB onto the substrate for static contact angle measurements. Measurements were repeated 5 times for each monomer on the PPFDA substrate, 4 times for HEMA on the PDVB substrate, and 3 times for each monomer on PPFOA and HEMA on P4VP and PHEMA.

The aspect ratio of nanodome height to diameter was measured using an Asylum Research MFP-3D-BIO atomic force microscope (AFM) in AC tapping mode. Scans were recorded across 1 x 1 μm and 0.5 Hz regions for each nanodome chemistry on the PPFDA and PDVB base layers. Scans were repeated in 4 different areas across the substrate and particles were selected with diameters in the range of 120-265 nm. The profile of the selected particles, 4 of each kind, were traced across the center of the dome to determine the end-to-end distance and base-to-tip height.

3. Results & Discussion

3.1 The Process of Condensed Droplet Polymerization (CDP)

CDP preparation involved the placement of a substrate (the surface of which we refer to as the "base layer" below, onto which condensation of monomer would occur) onto a thermoelectric cooler (TEC) module kept in a vacuum reactor chamber (Figure 1A).

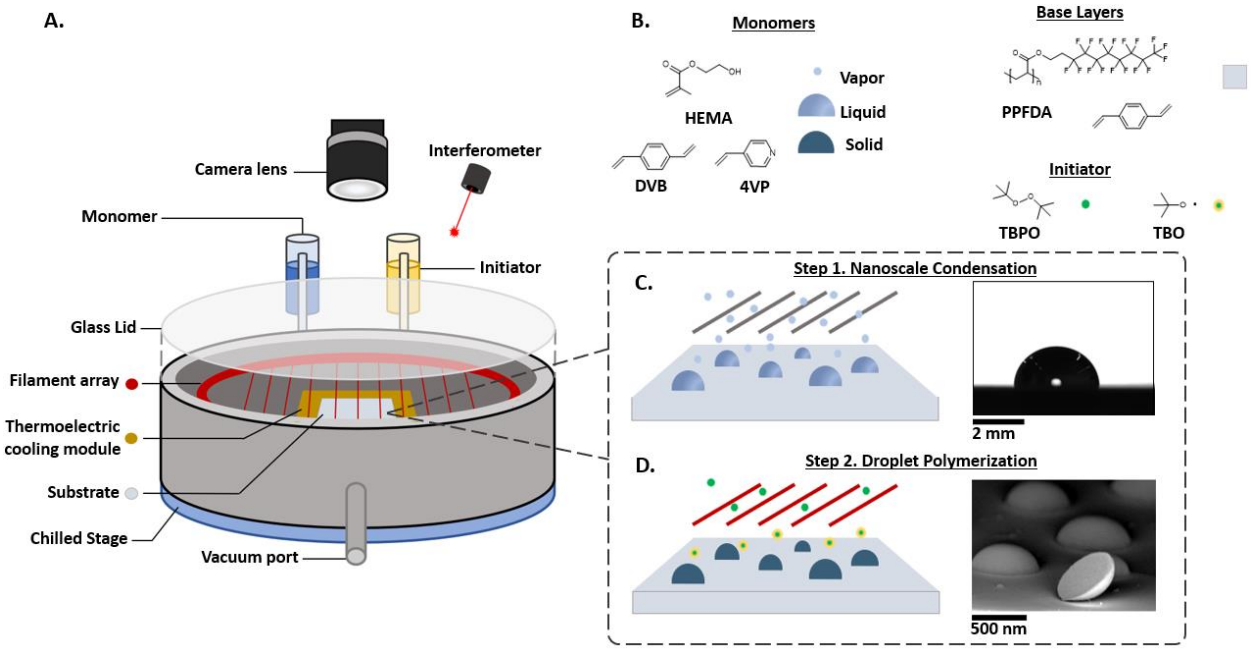

Figure 1. Vacuum reactor schematic and the CDP protocol. (A) An adapted iCVD reactor is depicted with components required for CDP, including a thermoelectric cooling (TEC) module (gold) on which the substrate sits for enhanced nanodrop formation and a digital microscope (top center) for in situ monitoring of the condensation-polymerization process. (B) Select monomers used to create polymer nanodomes are identified along with the chemistry of the substrate surface (referred to as the "base layer") and the polymerization initiator. (C) In the dashed box, the two steps of CDP are depicted. In Step 1, the vapor phase monomer condenses on the base layer (placed on the TEC module) to form nanoscale droplets. Dome-like shape was confirmed using macroscale goniometer measurements (5 µL liquid HEMA monomer on base layer, applied by pipette). (D) In Step 2, *tert*-butyl peroxide is delivered as a vapor and undergoes thermal decomposition to *tert*-butoxyl (TBO) and methyl radicals at a filament array (kept at 300 ºC). Impinging free radicals initiate polymerization of the condensed monomer droplet, solidifying the nanodomes in less than 45 seconds. SEM image of ndHEMA nanodomes (the use of "nd" before the monomer acronym

refers to the polymerized nanodome state) synthesized by the CDP technique shows the nanodome scale and the upturned particle confirms complete solidification (by polymerization) of the droplet.

The first step of CDP, i.e., nanoscale condensation, involved metering vapor of monomers into the evacuated reactor chamber (Figure 1C). Condensation of the monomer onto the base layer began once the pressure from monomer influx reached the saturation pressure at the substrate surface which was cooled by the TEC to below 10 °C. The rate of condensation is influenced by a multitude of parameters, including the thermodynamic properties of the monomer, surface energy of the base layer, temperature of the substrate, and thermal resistance between the TEC module and the condensing surface. Due to the extremely broad parameter space, we monitored Step 1 of CDP using real-time observation. We detected the onset and extent of condensation by two methods: (i) high-magnification digital microscopy in which condensed droplets appeared as dark spots, and (ii) in situ laser interferometry, the output of which diminished precipitously upon the formation of droplets due to laser scattering (Figure S2). These two methods combined exhibit condensation when droplets are below 200 nm in diameter, making the onset important to observe to create particles below 200 nm. Condensation was allowed to proceed by continued delivery of monomer vapor until the droplets of desired diameter were obtained, as determined by the photometer reading of the interferometer (e.g., a 5% decrease in photometer signal corresponded to nanodomes ~200 nm in diameter) and the real-time imaging using the digital microscope.

The second and final CDP step was a rapid polymerization of the droplets to solidify the liquid monomer into solid polymer nanodomes (Figure 1D). Vapor *tert*-butyl peroxide (TBPO)

was delivered (at 1.8 sccm) to the reactor chamber where thermal decomposition by a heated filament array at 300 °C generated *tert*-butoxyl (TBO) and methyl radicals. Impingement of TBO/methyl radicals onto the nanoscale condensed droplets initiated a free radical polymerization (Figure S3), solidifying the droplets as polymer nanodomes on the substrate surface within merely 45 seconds. The chamber was subsequently evacuated, and any unreacted species were removed to yield PNPs with high purity, as indicated by the materials characterization detailed below.

3.2 Physicochemical Properties of Nanodomes and Their Size Distribution

To assess PNPs with a variety of physicochemical properties, monomers selected for more extensive analysis included 4-vinylpyridine (4VP), divinylbenzene (DVB), and 2-hydroxyethyl methacrylate (HEMA) for hydrophilic and functionalizable [27], hydrophobic and crosslinked [30], and biocompatible[31] PNPs, respectively. Detailed characterization of the nanodomes first focuses on HEMA to exemplify the successful synthesis of polymer nanodomes by CDP, though any of the chemistries in Figure 1B may be analyzed by the same techniques. Below, we refer to polymer nanodomes and polymer thin films with "nd" and "P" preceding the name of the monomer, respectively (e.g., ndHEMA and PHEMA).

While the side-view (Figure 1D) and top-down (Figure 2A) SEM images illustrated the dome-shaped morphologies, energy dispersive x-ray spectroscopy (EDX) confirmed that the domes were also chemically distinct from the base layer, validating the condensation/dewetting-based mechanism of shape formation in CDP (Figure 2A). Larger ndHEMA with diameters around 10 μm were synthesized here due to the micron-scale resolution of the elemental mapping using EDX. Absence of fluorine atoms detected within the particles indicated that the particles were not

a morphological feature of the base layer [made of poly(1*H*,1*H*,2*H*,2*H*-perfluorodecyl acrylate) (PPFDA), the selection of which is discussed in Section 3.3], but a new material obtained via CDP. Oxygen atoms were concentrated where the domes were captured (in the top-down SEM image), which was consistent with the HEMA chemistry because the atomic percentage of oxygen in HEMA is triple that of PFDA (15.7% versus 5.1%).

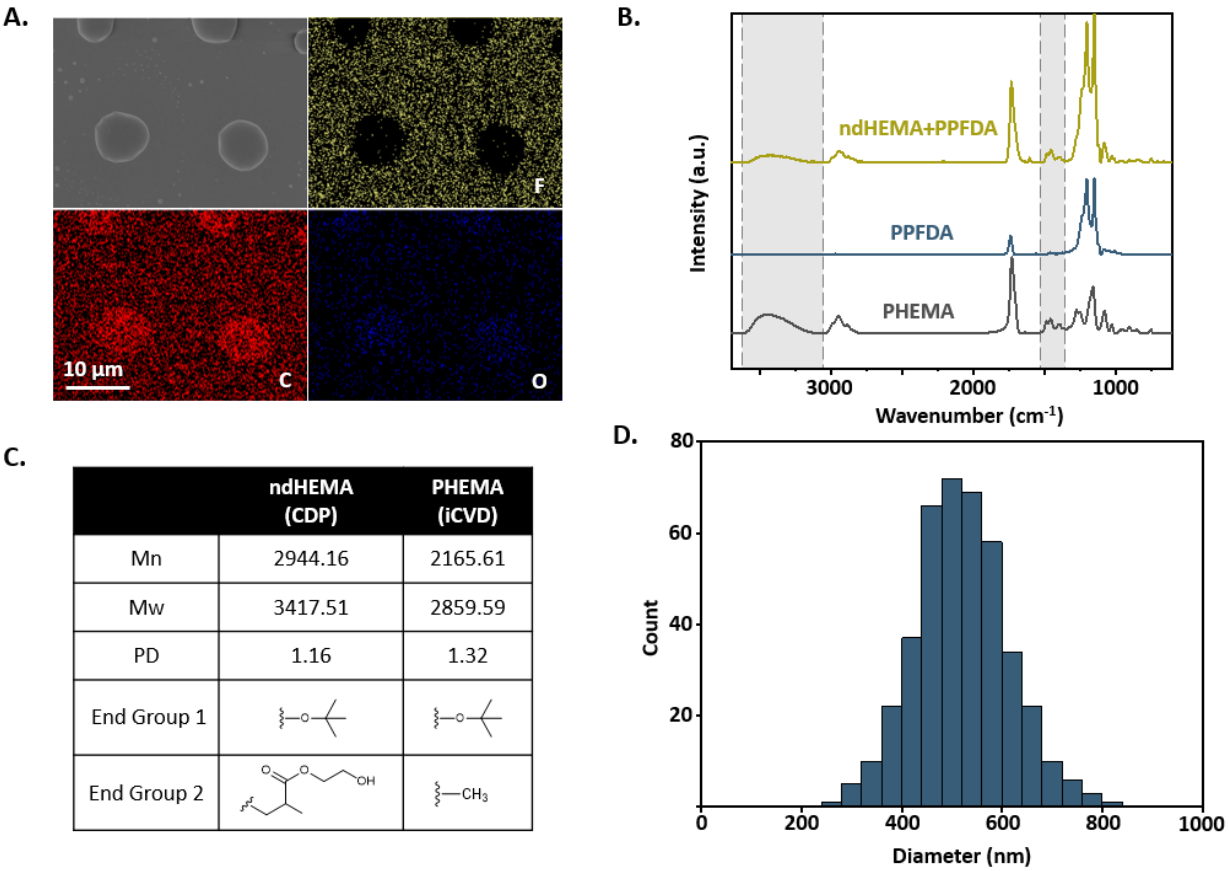

	ndHEMA (CDP)	PHEMA (iCVD)
Mn	2944.16	2165.61
Mw	3417.51	2859.59
PD	1.16	1.32
End Group 1		
End Group 2		

Figure 2. Chemical composition and size distribution of ndHEMA. (A) SEM image of ndHEMA (top left) with energy dispersive x-ray spectroscopy (EDX) mapping of fluorine (top right), carbon (bottom left), and oxygen (bottom right). (B) FTIR spectra of PHEMA (i.e., thin film; gray), PPFDA (i.e., the base layer; blue), and ndHEMA (i.e., nanodomes synthesized on top

of the base layer; gold). Gray background highlights the PHEMA peaks that are not present in the base layer, confirming successful polymerization during CDP. (C) Molecular weight and end group analysis of the PHEMA (synthesized using iCVD) and ndHEMA (synthesized using CDP), obtained using MALDI-TOF MS. (D) Histogram of ndHEMA diameters, measured from SEM images taken at 10 non-overlapping locations across the substrate of 416 distinct particles.

To confirm the chemical composition of the ndHEMA, we compared the Fourier transform infrared (FTIR) spectra of the PPFDA base layer, the ndHEMA atop the base layer (obtained using CDP), and PHEMA thin film (Figure 2B, see Figure S4 and Figure S5 for nd4VP and ndDVB spectra). Peaks associated with the base layer (blue) and PHEMA (gray) are preserved in the combined spectrum for the CDP-enabled ndHEMA on the base layer (gold) where peaks unique to PHEMA (i.e., ones that do not overlap with peaks from PPFDA) were highlighted with gray background. The broad peak above 3000 cm^{-1} identifies the O-H stretching and the peak at 1457 cm^{-1} associates with bending of C-H bond in the polymer backbone and the ethyl moiety of HEMA side chains [32,33]. Absent from each spectrum is a peak from C=C bonds (1660-1610 cm^{-1}) that signifies unreacted monomers, confirming the complete polymerization during CDP.

Indeed, despite the brief exposure to radicals (i.e., 45 seconds), complete polymerization was achieved even at the center of the dome base that is farthest from the liquid-vapor interface (where initiator radicals enter the monomer droplet), as demonstrated using SEM (Figure 1D). That rapid polymerization could be attributed to (i) the high concentration of monomers in the solvent-free nanodrop reaction system (see detailed discussion in the next paragraph); (ii) the vapor-delivered initiator radicals, which were abundant and diffused rapidly under vacuum, as

discussed below. Under the CDP conditions detailed in Section 2, within the first 10 seconds of step 2, the partial pressure of the initiator exceeded the partial pressure of the monomer in the vapor phase, effectively surrounding condensed monomer droplets with a vapor containing over 50% initiators (that were partially decomposed to radicals) and greatly accelerating the rate of polymerization. Furthermore, the radicals that entered monomer droplets were quickly replenished via the rapid arrival of radicals at the liquid-vapor interface, as their mean free path under the CDP conditions was ~300 μm, which was 6 orders of magnitude greater (see Supporting Information) than that in conventional, solution-based PNP synthesis (approximated to be less than one molecular diameter) [34]. Bulk polymerization of solvent-free monomers also leads to autoacceleration, i.e., the increase of the rate of polymerization with greater conversion of the monomer stock [35], due to local changes in viscosity that could contribute to the rapid polymerization [35,36].

The bulk and solvent-free polymerization mechanism, where pure monomer liquid undergoes polymerization, renders CDP fundamentally distinct from conventional CVD approaches, where polymerization occurs among vapor-phase or surface-adsorbed monomers. To unravel the impact of that difference in monomer concentration on the molecular structure of the resulting polymers, we compared ndHEMA (obtained via CDP) and PHEMA (obtained via iCVD) using matrix-assisted laser desorption ionization time-of-flight (MALDI-TOF) mass spectrometry (Figure 2C, Figure S6). MALDI-TOF analysis revealed an increase in polymer chain length and narrowed polydispersity index of the predominant chain type as a result of the high monomer molecule density in CDP [M_n = 2944.16 Da, M_w = 3417.51 Da, polydispersity index (PD) = 1.16] compared to iCVD (M_n = 2165.61 Da, M_w = 2859.59 Da, PD = 1.32). End group analysis revealed that PHEMA predominantly featured a *tert*-butoxide group at one end and a methyl group (methyl

radicals also form via β-scission at filament temperatures above 250 °C) at the other, whereas ndHEMA predominantly featured a *tert*-butoxide group at one end and a HEMA unit at the other end. While primary radical termination and recombination were considered main termination mechanisms in iCVD[37], the analysis of ndHEMA revealed that termination in CDP was instead dominated by disproportionation and/or chain transfer. The bulk polymerization inherent to the CDP technique supports this outcome because autoacceleration is known to generate heat that promotes chain transfer or disproportionation[35].

Diameters of ndHEMA demonstrated a Gaussian distribution with a coefficient of variation of 0.18 (Figure 2D; mean ± SD = 519 ± 92 nm), obtained using the SEM images of 416 unique ndHEMA nanodomes (synthesized using CDP with a target average diameter of 500 nm) and quantified using FIJI image analysis. The narrow size distribution obtained using CDP was likely a result of the coupled early-stage condensation and polymerization. Though more thoroughly studied in droplets over 1 μm in diameter, this is consistent with the initial growth stage of droplets following nucleation which is understood to be unimodal with a narrow size distribution[38]. This precedes the onset of coalescence and secondary nucleation when the size distribution broadens and becomes bimodal. Distinct from most condensation processes, CDP also relies on the polymerization step for PNP synthesis where the diminishment in polymerization kinetics due to limited diffusion length of radical species in a monomer drop generates a potential cut-off particle size, enabling the synthesis of PNPs with narrow size distributions using CDP[39]. The systematic investigation of the dispersity of PNP diameters as a function of the CDP synthesis conditions, monomer surface tension, and properties of the radical species, will be reserved for future studies.

3.3 Controlling the Aspect Ratio of the Nanodomes via Base Layer Engineering

Dimension programmability, illustrated here as control over the height-to-width ratio of the nanodomes (Figure 3, where width indicates diameter of the dome base), was enabled by tuning the surface energy of the base layer. While we focused on smooth base layers that gave rise to spherical dome bases to deconvolute PNP shape from structural features of the base layer and thereby unravel the effect of interfacial energy on PNP shape, non-spherical dome bases could be easily obtained using structured base layers, such as those obtained using standard lithography techniques [40].

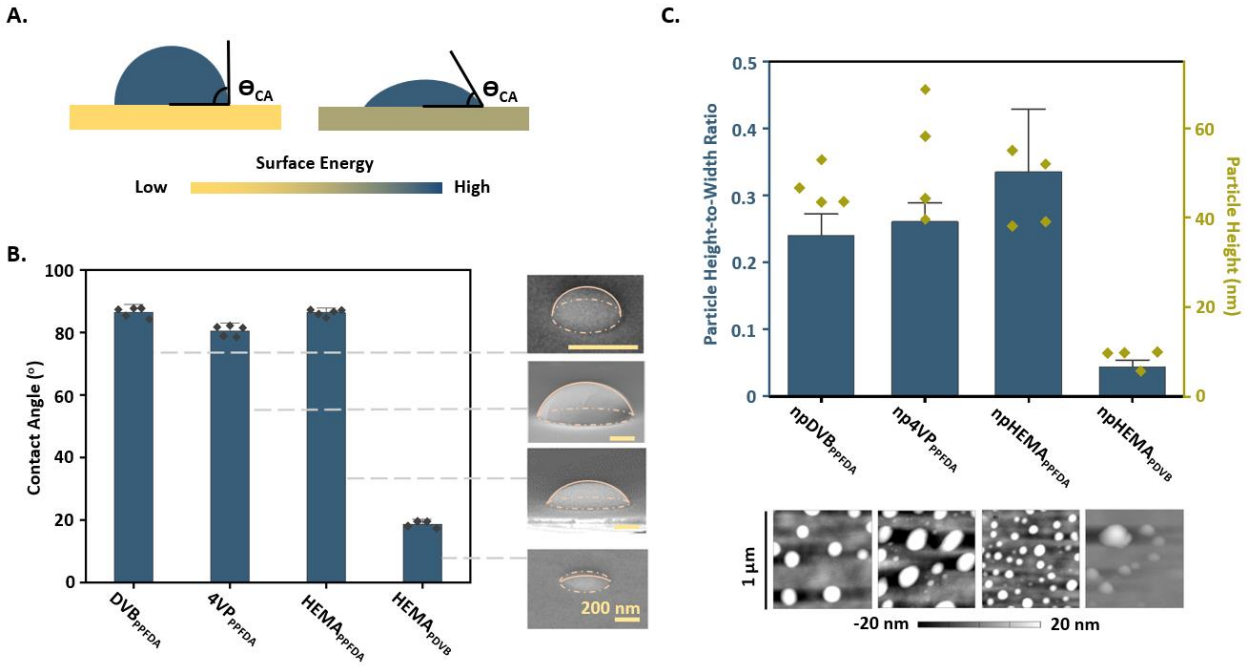

Figure 3. Programming polymer nanodome dimensions through controlled dewetting. (A) Tuning the base layer surface energy leads to controlled contact angle (Θ_{CA}) of the liquid monomer

upon condensation and thus programmable height-to-width ratio of the PNPs. (B) Contact angles of a range of liquid monomers (standard script) on the base layer of PPFDA (subscript, representing low surface-energy base layer) and that of HEMA on a PDVB base layer (subscript, representing high surface-energy base layer) (n = 5 for all monomers on PPFDA; n = 4 for HEMA on PDVB), which were comparable to the side angle profiles of the nanodomes illustrated by SEM images, where the dome base and the outer edge of the dome surface were traced by tan dotted and solid lines, respectively, for clarity. (C) Height (gold diamonds, right y-axis) and height-to-width ratios (blue bars, left y-axis, data represents mean ± SD) of the nanodomes measured by AFM tracing (n = 4), and the AFM images (bottom images), where the ndHEMA nanodomes on the PDVB base layer demonstrated much lower heigh-to-width ratio than that on the PPFDA base layer. All nanodomes were synthesized with a similar diameter at the dome base.

On a smooth base layer, a low interfacial energy was anticipated to enhance dewetting by a condensed monomer droplet, thus yielding a high contact angle and a large height-to-width ratio of the nanodomes, and vice versa (Figure 3A). The flat base layer was obtained by depositing on flat silicon (Si) wafers a 100-to-200-nm-thick layer of PPFDA (with the surface energy of ~9 mN m^{-1})[41] or of poly(DVB) (PDVB, with the surface energy of ~29 mN m^{-1})[41] using the conventional iCVD technique [27]. The boundary between dropwise and filmwise condensation is multifactorial and important to consider given that dropwise condensation is necessary for PNP formation [42]. For the monomers chosen here that achieve dropwise condensation, the contact angle can be used to assess the degree of dewetting and corresponding aspect ratio of the nanodomes.

PPFDA thin films are known to give rise to surfaces that are superhydrophobic, oleophobic, and/or repellant of most liquids [43], making them a good choice for base layer to obtain dropwise condensation with most monomers. Contact angles were recorded for monomers DVB, 4VP, and HEMA on the PPFDA base layer as 86.4 ± 1.0°, 80.6 ± 1.7°, and 86.5 ± 1.6° respectively (Figure 3B). Side-view SEM images confirmed the near 90° contact angles and equivalent dome-shaped profiles of the PNPs from each monomer type. The height-to-width ratio of the nanodomes was quantified via profile tracing using atomic force microscopy (AFM, Figure 3C), where ndDVB, nd4VP, and ndHEMA exhibited values of 0.24 ± 0.021, 0.26 ± 0.019, and 0.33 ± 0.063 respectively. To raise the surface energy of the base layer, HEMA was condensed on a PDVB base layer and exhibited a contact angle of 18.5 ± 1.1°, merely 21% the contact angle of HEMA on the PPFDA base layer. The resulting ndHEMA observed in SEM were flatter, with a substantially lower height-to-width ratio (0.043 ± 0.0072) than that of ndHEMA on PPFDA (0.33 ± 0.063).

Importantly, this confirmed a reliable correlation between the contact angles of macroscale monomer droplets (measurable with a goniometer) with nanoscale PNPs (which were observable with SEM and AFM post-polymerization). While deviation of contact angles at single-digit nanometer scale from that measured macroscopically is well-characterized [44,45], the monomer droplets reported here maintained consistent contact angles across length scales, likely due to their sizes being over 10 nm. Despite a potential volume change upon polymerization, the consistency of contact angles spanning the macroscale to the nanoscale, and between liquid monomers and polymerized particles, enabled prediction and thus potential shape programming of the PNPs obtained using CDP. That PNP shape/dimension programming could be accomplished by selection of a desired base layer and monomer pair through contact angle goniometry. To demonstrate the tunability of the monomer contact angle and thereby the aspect ratio of the polymer nanodomes,

we recorded the contact angles of HEMA, DVB, and 4VP on poly(1*H*,1*H*,2*H*,2*H*-perfluorooctyl acrylate) (PPFOA), as well as HEMA on the homopolymers of P4VP and PHEMA to complement the data in Figure 3B (Figure S7). The shorter perfluorinated chain of PPFOA compared to PPFDA yielded lower contact angles in the range of 42-72° and the contact angle of HEMA on P4VP was approximately 30°. Taken together, the contact angles of each monomer on the two perfluorinated base layers and HEMA on each homopolymer base layer (i.e., PPFDA, PPFOA, P4VP, PDVB, and PHEMA) span the range of 18-86° and the choice of one monomer-base layer pair could be used to control the resultant particle aspect ratio. Such control is facile compared to laborious nanoscale templating (e.g., lithography) or the multi-day solution-based synthesis (e.g., in the case of nanodomes derived from Janus particles). CDP has the added benefit of unimpeded droplet spreading across a flat base layer to produce low aspect ratios that would be challenging in the aforementioned templated alternatives.

Following CDP, the nanodomes could be dislodged from the base layer as individual particles by mechanical force (e.g., scraping, rinsing, or sonication) while retaining the established shape and dimensions as demonstrated with ndDVB (Figure S8).

3.4 Independent Control of Nanodome Chemistry and Diameter via In-Situ and Real-Time Monitoring

In addition to the programmable aspect ratio demonstrated above with nanodomes synthesized using a variety of monomer types (e.g., cross-linker and functionalizable, hydrophilic and biocompatible ones), the size versatility of the CDP approach was demonstrated by creating nanodomes with diameters spanning the full nanometer size range and up to ~1 μm (Figure 4).

The diameter of CDP nanodomes were controlled by monitoring the growth of monomer droplets (during the condensation step) with interferometry and the in-situ microscopy, which was demonstrated effective regardless of the monomer type. As such, CDP can synthesize nanodomes of any nanoscale diameter with no need to modify the CDP protocol. This stands in contrast to existing methods like the self-assembly of block copolymers, which are limited to a size that is predetermined by the length and self-assembly behavior of the block copolymer chains, or protocols that rely on rigid microfluidic devices [46,47]. Though nano-sized particles are more common in applications like drug delivery [48], we have also created domes that are tens of microns in diameter (see Figure 2A). Within the size range investigated in this study, all condensed monomer droplets fully polymerized; and a potential upper bound of CDP particle size, above which complete polymerization may not occur, will be an interesting focus in future studies on micrometer- to millimeter-scale domes synthesized using CDP.

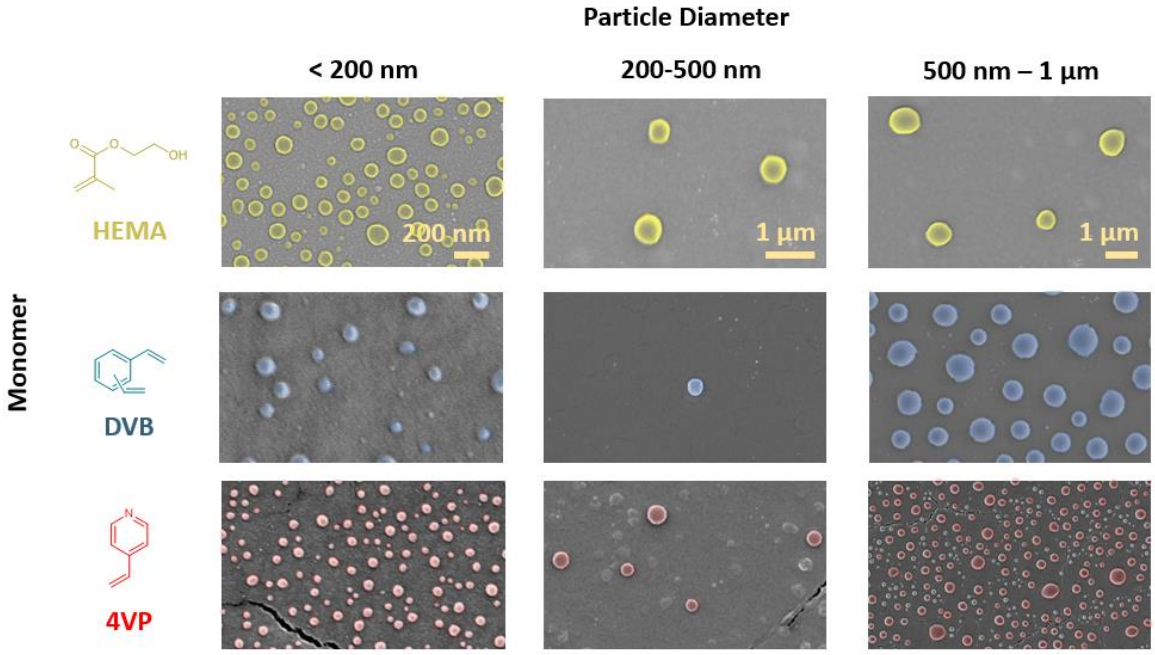

Figure 4. Polymer nanodomes with multiple chemical functionalities and sizes that were enabled by the CDP technique by controlled extent of condensation. SEM images exhibit the versatility of CDP which yields nanodomes from three monomer types, giving rise to PNPs that were crosslinked, functionalizable, hydrophilic, and/or biocompatible, and with diameters of each spanning the full nanoscale. PNPs of the same chemistry are grouped by row and pseudo-colored for clarity against the base layer (i.e., the gray surroundings). Domes with diameters spanning the full nanoscale range are grouped by column.

Finally, the chemical versatility of the CDP approach was further demonstrated through the synthesis and characterization of polymer nanodomes from six additional monomers (Figure 5). Synthesizing nanodomes of a different polymer type requires no adaptation of the CDP protocol detailed above. By simply delivering the corresponding monomer to the reactor, CDP was used to successfully obtain nanodomes of poly(glycidyl methacrylate) (ndGMA), poly(benzyl methacrylate) (ndBMA), poly(ethylene glycol dimethacrylate) (ndEGDMA), poly(1-vinylimidazole) (nd1VI), poly(cyclohexyl methacrylate) (ndCHMA), and poly[2-(dimethylamino)ethyl methacrylate] (ndDMAEMA), as shown in the SEM images of Figure 5. This set of monomers collectively includes crosslinking agents (EGDMA, GMA), functionalizable epoxide groups (GMA), aromatic rings (BMA, 1VI), and secondary and tertiary amines (1VI, DMAEMA), among other characteristics that yield polymers with unique physicochemical properties and/or opportunities for side chain functionalization.

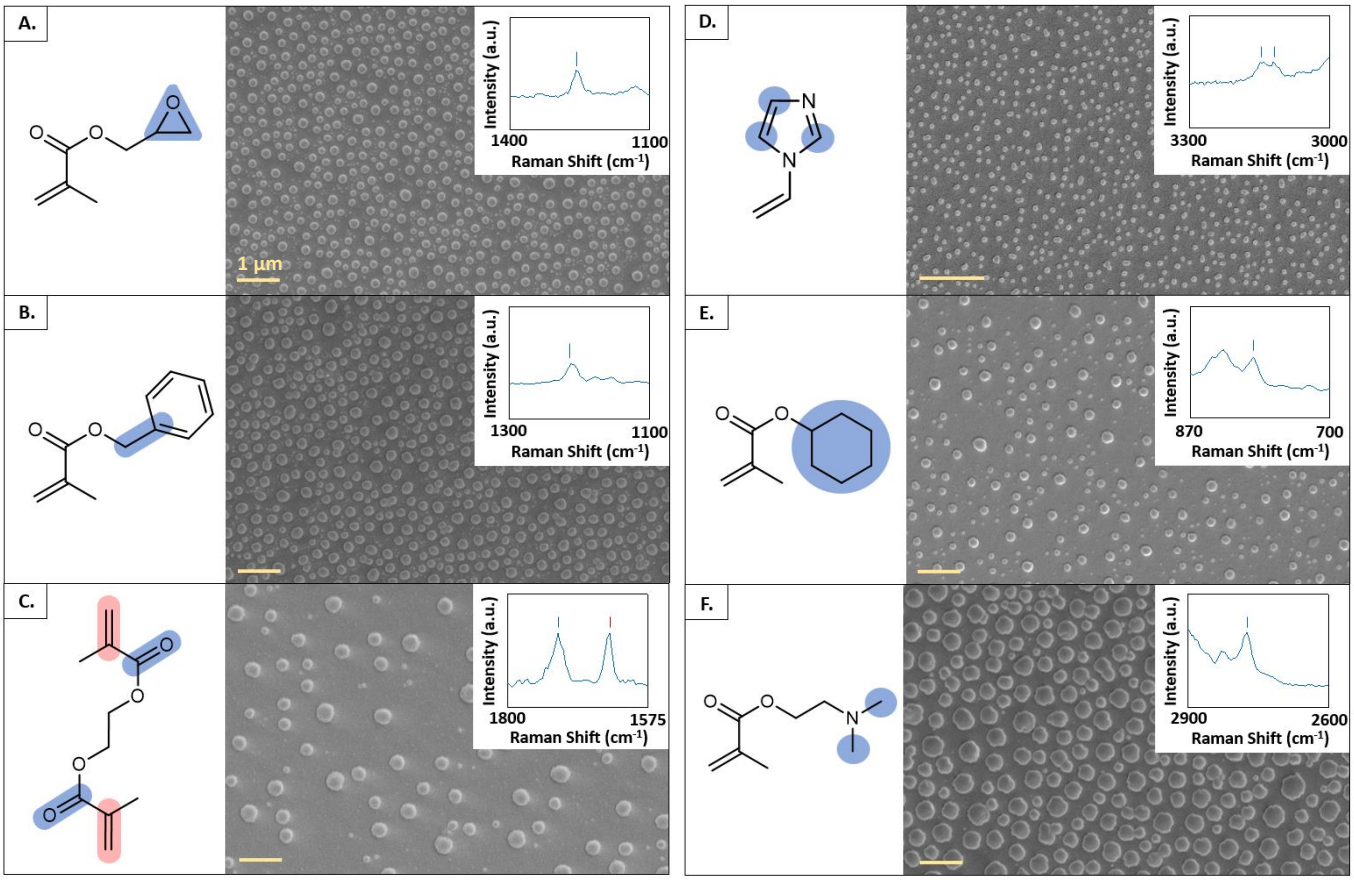

Figure 5. Polymer nanodomes synthesized using a variety of monomer chemistries without alteration of the CDP technique. SEM images of polymer particles (right) with the chemical structure of the corresponding monomer (left) and signature peaks in the Raman spectrum (inset) for (A) glycidyl methacrylate, (B) benzyl methacrylate, (C) ethylene glycol dimethacrylate, (D) 1-vinylimidazole, (E) cyclohexyl methacrylate, and (F) 2-(dimethylamino)ethyl methacrylate. All scale bars are 1 µm.

Confocal Raman microscopy was used to confirm the chemical composition of the polymer nanodomes synthesized using the library of monomers. It enables the compositional analyses of

individual particles by coupling a Raman spectrometer to a confocal microscope, thus achieving simultaneous high-magnification visualization and Raman analysis. Polymer domes were synthesized with diameters in the single-digit micrometer range for analyses using confocal Raman microscopy because the typical spatial resolution of Raman microscopy is on the order of 1 μm. Spectra in Figure 5 highlight the Raman peaks that are characteristic of a functional group that is signature of each monomer. Specifically, the peak at 1259 cm^{-1} observed in ndGMA result from the stretch of the epoxide ring (Figure 5A)[49]; ndBMA exhibited a peak at 1210 cm^{-1} that is characteristic of the C_6H_5-C vibration of the benzyl moiety (Figure 5B)[50]; the peak at 1721 cm^{-1} corresponding to the C=O stretch of ndEGDMA (Figure 5C) is importantly accompanied by a peak at 1640 cm^{-1}, which is due to the pendant vinyl bonds of the crosslinking EGDMA monomer [51]. The vinyl peak is not observed in the nanodomes formed by non-crosslinking monomers because those monomers were fully polymerized during CDP, as confirmed previously (Figure 1D), The Raman spectrum of nd1VI displayed peaks at 3118 cm^{-1} and 3138 cm^{-1} that identified C-H bonds in the imidazole ring (Figure 5D)[52]; the peak at 795 cm^{-1} in Figure 5E was attributed to the breathing mode of the cyclohexyl group of poly(CHMA)[53]. Poly(DMAEMA) showed a peak at 2776 cm^{-1} that is characteristic of the terminal CH_3 groups (Figure 5F)[54].

4. Conclusions

In this work, we have introduced a new method for bottom-up synthesis of PNPs, using polymer nanodomes as a proof-of-principle. The CDP approach is unprecedented in its template- and solvent-free nature, as well as its rapidity and versatility. This solvent-free technique is unhindered by monomer solubility concerns and is thus amenable to virtually any monomer types without the need for changes to the technique or synthesis conditions, as exemplified by the

nanodomes comprised of nine different polymers demonstrated in this work. Moreover, CDP is capable of producing domes of each chemistry at sizes from below 20 nm to above 1 μm. By simply tuning the surface energy of the base layer, the height-to-width ratios of the resulting nanodomes can be controlled. Furthermore, CDP polymerization is complete in less than 45 seconds, compared to hours- or days-long procedures used in existing PNP synthesis protocols.

CDP is also versatile due to its amenability to adaptions that accommodate unique properties of the monomers or would produce non-spherical, non-dome shapes that we discuss below but have reserved for future studies. The heated filament array and TBPO initiator, for example, could be replaced by a ultraviolet (UV) lamp to initiate UV-photopolymerizable monomers and provide access to nanoparticle synthesis within cavities or other non-line-of-sight surfaces. When condensed droplets form on the substrate, their base shape could be defined by physical structures on the surface. By using base layers with patterned wetting properties or structural features, CDP has the potential to produce anisotropic and non-spherical PNPs, enabling novel and impactful applications; for example, rod-shaped nanoparticles have been shown to have longer residence time in cells than spheres which could be leveraged to program the pharmacokinetics of *in vivo* drug delivery systems [55]. To bolster the applicability of CDP to new technologies, future studies should address limitations in the understanding of condensation behavior of monomers. Parameters that influence condensation will influence on the droplet dispersity and surface density and could change from monomer to monomer. Furthermore, droplets can be expected to have a maximum size such that complete polymerization is not possible due to the formation of an impenetrable polymerized shell. This critical size should be studied for each monomer in order to consider applications in the microscale and could be altered by the implementation of other initiator types with higher diffusivity in the condensed monomer droplets.

Having surmounted the barriers of conventional solution-based synthesis approaches, which are often time-consuming and chemistry- and/or size-restrictive, CDP represents a new paradigm in soft nanomaterials research. The polymeric nanodomes alone offer exciting new research avenues in self-assembly and jamming properties important to soft robotics (such as haptics) [56] and injectable implants [57]. The rapid and scalable CDP process has the potential to transform the manufacturing and deployment of polymeric nanomaterials.

Acknowledgments:

Analytical methods involved use of the Cornell Center for Materials Research (CCMR) Shared Facilities which are supported through the NSF MRSEC program (DMR-1719875). This material is based upon work supported by the National Science Foundation Graduate Research Fellowship Program under Grant No. DGE-1650441 and the National Science Foundation Faculty Early Career Development Program under Grant No. CMMI-2144171. Any opinions, findings, and conclusions or recommendations expressed in this material are those of the author(s) and do not necessarily reflect the views of the National Science Foundation.

Supporting Information Available: Mean free path calculation, protocol for and SEM imaging of base layer flattening, interferometry- and microscopy-based in situ observation of condensation, free radical polymerization scheme for CDP monomers, FTIR spectra identifying nd4VP nanodomes, FTIR spectra identifying ndDVB nandomes, MALDI-TOF spectra, contact angle of monomers on alternative base layers, SEM imaging of isolated ndDVB nanodomes, This material is available free of charge *via* the Internet at http://pubs.acs.org.

Corresponding Author:

Rong Yang – ryang@cornell.edu

Author Contributions:

T.F. and D.S. conducted the CDP syntheses. T.F. performed all other experiments. T.F. and R.Y. contributed to the study design and data analysis. T.D., D.S., and R.Y. drafted the manuscript and edited it for critically important intellectual content.

References:

(1) Dendukuri, D.; Pregibon, D. C.; Collins, J.; Hatton, T. A.; Doyle, P. S. Continuous-Flow Lithography for High-Throughput Microparticle Synthesis. *Nat. Mater.* **2006**, *5* (5), 365–369.

(2) Lesov, I.; Valkova, Z.; Vassileva, E.; Georgiev, G. S.; Ruseva, K.; Simeonov, M.; Tcholakova, S.; Denkov, N. D.; Smoukov, S. K. Bottom-Up Synthesis of Polymeric Micro- and Nanoparticles with Regular Anisotropic Shapes. *Macromolecules* **2018**, *51* (19), 7456–7462.

(3) Banik, B. L.; Fattahi, P.; Brown, J. L. Polymeric Nanoparticles: The Future of Nanomedicine. *WIREs Nanomedicine and Nanobiotechnology* **2016**, *8* (2), 271–299.

(4) Haryadi, B. M.; Hafner, D.; Amin, I.; Schubel, R.; Jordan, R.; Winter, G.; Engert, J. Nonspherical Nanoparticle Shape Stability Is Affected by Complex Manufacturing Aspects: Its Implications for Drug Delivery and Targeting. *Adv. Healthc. Mater.* **2019**, *8* (18), 1900352.

(5) Fish, M. B.; Thompson, A. J.; Fromen, C. A.; Eniola-Adefeso, O. Emergence and Utility of Nonspherical Particles in Biomedicine. *Ind. Eng. Chem. Res.* **2015**, *54* (16), 4043–4059.

(6) Taranekar, P.; Park, J.-Y.; Patton, D.; Fulghum, T.; Ramon, G. J.; Advincula, R. Conjugated Polymer Nanoparticles via Intramolecular Crosslinking of Dendrimeric Precursors. *Adv. Mater.* **2006**, *18* (18), 2461–2465.

(7) Anselmo, A. C.; Mitragotri, S. Nanoparticles in the Clinic: An Update. *Bioeng. Transl. Med.* **2019**, *4* (3), e10143.

(8) Wu, H.-Y.; Cunningham, B. T. Point-of-Care Detection and Real-Time Monitoring of Intravenously Delivered Drugs via Tubing with an Integrated SERS Sensor. *Nanoscale* **2014**, *6* (10), 5162–5171.

(9) Yamashita, N.; Konishi, N.; Tanaka, T.; Okubo, M. Preparation of Hemispherical Polymer Particles by Cleavage of a Janus Poly(Methyl Methacrylate) /Polystyrene Composite Particle†Part CCCLVII of the Series "Studies on Suspension and Emulsion". *Langmuir* **2012**, *28* (35), 12886–12892.

(10) Chen, W.-H.; Tu, F.; Bradley, L. C.; Lee, D. Shape-Tunable Synthesis of Sub-Micrometer Lens-Shaped Particles via Seeded Emulsion Polymerization. *Chem. Mater.* **2017**, *29* (7), 2685–2688.

(11) Park, H.-Y.; Jang, I.; Jung, N.; Chung, Y.-H.; Ryu, J.; Cha, I. Y.; Kim, H.-J.; Jang, J. H.; Yoo, S. J. Green Synthesis of Carbon-Supported Nanoparticle Catalysts by Physical Vapor Deposition on Soluble Powder Substrates. *Sci. Rep.* **2015**, *5* (1), 14245.

(12) Yu, F.; Xu, J.; Li, H.; Wang, Z.; Sun, L.; Deng, T.; Tao, P.; Liang, Q. Ga-In Liquid Metal Nanoparticles Prepared by Physical Vapor Deposition. *Prog. Nat. Sci. Mater. Int.* **2018**, *28* (1), 28–33.

(13) Pandey, P. A.; Bell, G. R.; Rourke, J. P.; Sanchez, A. M.; Elkin, M. D.; Hickey, B. J.; Wilson, N. R. Physical Vapor Deposition of Metal Nanoparticles on Chemically Modified Graphene: Observations on Metal–Graphene Interactions. *Small* **2011**, *7* (22), 3202–3210.

(14) Rao, J. P.; Geckeler, K. E. Polymer Nanoparticles: Preparation Techniques and Size-Control Parameters. *Prog. Polym. Sci.* **2011**, *36* (7), 887–913.

(15) Sundberg, D. Structured, Composite Nanoparticles from Emulsion Polymerization – Morphological Possibilities. *Biomacromolecules*. American Chemical Society August 30, 2020.

(16) Gharieh, A.; Khoee, S.; Mahdavian, A. R. Emulsion and Miniemulsion Techniques in Preparation of Polymer Nanoparticles with Versatile Characteristics. *Adv. Colloid Interface Sci.* **2019**, *269*, 152–186.

(17) Yanagishita, T.; Fujimura, R.; Nishio, K.; Masuda, H. Fabrication of Monodisperse Polymer Nanoparticles by Membrane Emulsification Using Ordered Anodic Porous Alumina. *Langmuir* **2010**, *26* (3), 1516–1519.

(18) Wurm, F. R.; Weiss, C. K. Nanoparticles from Renewable Polymers. *Front. Chem.* **2014**, *2*, 49.

(19) Piszczek, P. Silver Nanoparticles Fabricated Using Chemical Vapor Deposition and Atomic Layer Deposition Techniques: Properties, Applications and Perspectives: Review; Bristow, A. R. E.-M. S. S. E.-A. D., Ed.; IntechOpen: Rijeka, 2018; pp 187–213.

(20) De Filpo, G.; Pantuso, E.; Armentano, K.; Formoso, P.; Di Profio, G.; Poerio, T.; Fontananova, E.; Meringolo, C.; Mashin, A. I.; Nicoletta, F. P. Chemical Vapor Deposition of Photocatalyst Nanoparticles on PVDF Membranes for Advanced Oxidation Processes. *Membranes (Basel).* **2018**, *8* (3), 35.

(21) Cheng, K. C. K.; Bedolla-Pantoja, M. A.; Kim, Y.-K.; Gregory, J. V; Xie, F.; de France, A.; Hussal, C.; Sun, K.; Abbott, N. L.; Lahann, J. Templated Nanofiber Synthesis via Chemical Vapor Polymerization into Liquid Crystalline Films. *Science (80-.).* **2018**, *362* (6416), 804

LP – 808.

(22) Haller, P. D.; Gupta, M. Synthesis of Polymer Nanoparticles via Vapor Phase Deposition onto Liquid Substrates. *Macromol. Rapid Commun.* **2014**, *35* (23), 2000–2004.

(23) Wei, X.; Sbalbi, N.; Bradley, L. C. Nematic Colloids at Liquid Crystal–Air Interfaces via Photopolymerization. *Soft Matter* **2020**, *16* (39), 9121–9127.

(24) Tung, H.-Y.; Guan, Z.-Y.; Liu, T.-Y.; Chen, H.-Y. Vapor Sublimation and Deposition to Build Porous Particles and Composites. *Nat. Commun.* **2018**, *9* (1), 2564.

(25) Pereira, A. do E. S.; Oliveira, H. C.; Fraceto, L. F. Polymeric Nanoparticles as an Alternative for Application of Gibberellic Acid in Sustainable Agriculture: A Field Study. *Sci. Rep.* **2019**, *9* (1), 7135.

(26) Abdul Rahman, N. Applications of Polymeric Nanoparticles in Food Sector BT - Nanotechnology: Applications in Energy, Drug and Food; Siddiquee, S., Melvin, G. J. H., Rahman, M. M., Eds.; Springer International Publishing: Cham, 2019; pp 345–359.

(27) Donadt, T. B.; Yang, R. Amphiphilic Polymer Thin Films with Enhanced Resistance to Biofilm Formation at the Solid–Liquid–Air Interface. *Adv. Mater. Interfaces* **2021**, *5* (8), 2001791.

(28) Coclite, A. M.; Shi, Y.; Gleason, K. K. Controlling the Degree of Crystallinity and Preferred Crystallographic Orientation in Poly-Perfluorodecylacrylate Thin Films by Initiated Chemical Vapor Deposition. *Adv. Funct. Mater.* **2012**, *22* (10), 2167–2176.

(29) Christian, P.; Coclite, A. M. Vapor-Phase-Synthesized Fluoroacrylate Polymer Thin Films: Thermal Stability and Structural Properties. *Beilstein J. Nanotechnol.* **2017**, *8*, 933–942.

(30) Zhao, J.; Wang, M.; Gleason, K. K. Stabilizing the Wettability of Initiated Chemical Vapor Deposited (ICVD) Polydivinylbenzene Thin Films by Thermal Annealing. *Adv. Mater. Interfaces* **2017**, *4* (18), 1700270.

(31) Zare, M.; Bigham, A.; Zare, M.; Luo, H.; Rezvani Ghomi, E.; Ramakrishna, S. PHEMA: An Overview for Biomedical Applications. *Int. J. Mol. Sci.* **2021**, *22* (12), 6376.

(32) Pfluger, C. A.; Carrier, R. L.; Sun, B.; Ziemer, K. S.; Burkey, D. D. Cross-Linking and Degradation Properties of Plasma Enhanced Chemical Vapor Deposited Poly(2-Hydroxyethyl Methacrylate). *Macromol. Rapid Commun.* **2009**, *30* (2), 126–132.

(33) Cheng, Y.; Khlyustova, A.; Chen, P.; Yang, R. Kinetics of All-Dry Free Radical Polymerization under Nanoconfinement. *Macromolecules* **2020**, *53* (24), 10699–10710.

(34) Lovell, P. A.; Schork, F. J. Fundamentals of Emulsion Polymerization. *Biomacromolecules* **2020**, *21* (11), 4396–4441.

(35) Odian, G. Radical Chain Polymerization. In *Principles of Polymerization*; Wiley Online Books; 2004; pp 198–349.

(36) Jašo, V.; Stoiljković, D.; Radičević, R.; Bera, O. Kinetic Modeling of Bulk Free-Radical Polymerization of Methyl Methacrylate. *Polym. J.* **2013**, *45* (6), 631–636.

(37) Khlyustova, A.; Yang, R. Initiated Chemical Vapor Deposition Kinetics of Poly(4-Aminostyrene). *Front. Bioeng. Biotechnol.* **2021**, *9*, 309.

(38) Stricker, L.; Grillo, F.; Marquez, E. A.; Panzarasa, G.; Smith-Mannschott, K.; Vollmer, J. Universality of Breath Figures on Two-Dimensional Surfaces: An Experimental Study. *Phys. Rev. Res.* **2022**, *4* (1), L012019.

(39) Wei, Z.; Li, Y.; Cooks, R. G.; Yan, X. Accelerated Reaction Kinetics in Microdroplets: Overview and Recent Developments. *Annu. Rev. Phys. Chem.* **2020**, *71* (1), 31–51.

(40) Qin, D.; Xia, Y.; Whitesides, G. M. Soft Lithography for Micro- and Nanoscale Patterning. *Nat. Protoc.* **2010**, *5* (3), 491–502.

(41) Zhao, J.; Wang, M.; Jebutu, M. S.; Zhu, M.; Gleason, K. K. Fundamental Nanoscale Surface Strategies for Robustly Controlling Heterogeneous Nucleation of Calcium Carbonate. *J. Mater. Chem. A* **2019**, *7* (29), 17242–17247.

(42) Zheng, S.-F.; Gross, U.; Wang, X.-D. Dropwise Condensation: From Fundamentals of Wetting, Nucleation, and Droplet Mobility to Performance Improvement by Advanced Functional Surfaces. *Adv. Colloid Interface Sci.* **2021**, *295*, 102503.

(43) Coclite, A. M.; Shi, Y.; Gleason, K. K. Super-Hydrophobic and Oloephobic Crystalline Coatings by Initiated Chemical Vapor Deposition. *Phys. Procedia* **2013**, *46*, 56–61.

(44) Khalkhali, M.; Kazemi, N.; Zhang, H.; Liu, Q. Wetting at the Nanoscale: A Molecular Dynamics Study. *J. Chem. Phys.* **2017**, *146* (11), 114704.

(45) Zhang, J.; Wang, P.; Borg, M. K.; Reese, J. M.; Wen, D. A Critical Assessment of the Line Tension Determined by the Modified Young's Equation. *Phys. Fluids* **2018**, *30* (8), 82003.

(46) Robb, M. J.; Connal, L. A.; Lee, B. F.; Lynd, N. A.; Hawker, C. J. Functional Block Copolymer Nanoparticles: Toward the next Generation of Delivery Vehicles. *Polym. Chem.* **2012**, *3* (6), 1618–1628.

(47) Hasani-Sadrabadi, M. M.; Majedi, F. S.; VanDersarl, J. J.; Dashtimoghadam, E.; Ghaffarian, S. R.; Bertsch, A.; Moaddel, H.; Renaud, P. Morphological Tuning of Polymeric

Nanoparticles via Microfluidic Platform for Fuel Cell Applications. *J. Am. Chem. Soc.* **2012**, *134* (46), 18904–18907.

(48) Mitchell, M. J.; Billingsley, M. M.; Haley, R. M.; Wechsler, M. E.; Peppas, N. A.; Langer, R. Engineering Precision Nanoparticles for Drug Delivery. *Nat. Rev. Drug Discov.* **2021**, *20* (2), 101–124.

(49) Boerio, F. J.; Yuann, J. K. Determination of Copolymer Composition by Raman Spectroscopy. *J. Polym. Sci. Polym. Phys. Ed.* **1973**, *11* (9), 1841–1848.

(50) Barnes, S. E.; Cygan, Z. T.; Yates, J. K.; Beers, K. L.; Amis, E. J. Raman Spectroscopic Monitoring of Droplet Polymerization in a Microfluidic Device. *Analyst* **2006**, *131* (9), 1027–1033.

(51) Socrates, G. *Infrared and Raman Characteristic Group Frequencies: Tables and Charts*, 3rd ed.; John Wiley & Sons, Ltd: Chichester, 2001.

(52) Talu, M.; Demiroğlu, E. U.; Yurdakul, Ş.; Badoğlu, S. FTIR, Raman and NMR Spectroscopic and DFT Theoretical Studies on Poly(N-Vinylimidazole). *Spectrochim. Acta Part A Mol. Biomol. Spectrosc.* **2015**, *134*, 267–275.

(53) Lin-Vien, D.; Colthup, N. B.; Fateley, W. G.; Grasselli, J. G. CHAPTER 2 - Alkanes; Lin-Vien, D., Colthup, N. B., Fateley, W. G., Grasselli, J. G. B. T.-T. H. of I. and R. C. F. of O. M., Eds.; Academic Press: San Diego, 1991; pp 9–28.

(54) Contreras-García, A.; Bucio, E.; Brackman, G.; Coenye, T.; Concheiro, A.; Alvarez-Lorenzo, C. Biofilm Inhibition and Drug-Eluting Properties of Novel DMAEMA-Modified Polyethylene and Silicone Rubber Surfaces. *Biofouling* **2011**, *27* (2), 123–135.

(55) Wang, W.; Gaus, K.; Tilley, R. D.; Gooding, J. J. The Impact of Nanoparticle Shape on Cellular Internalisation and Transport: What Do the Different Analysis Methods Tell Us? *Mater. Horizons* **2019**, *6* (8), 1538–1547.

(56) Peng, Y.; Serfass, C. M.; Kawazoe, A.; Shao, Y.; Gutierrez, K.; Hill, C. N.; Santos, V. J.; Visell, Y.; Hsiao, L. C. Elastohydrodynamic Friction of Robotic and Human Fingers on Soft Micropatterned Substrates. *Nat. Mater.* **2021**, *22*, 1707–1711.

(57) Feig, V. R.; Santhanam, S.; McConnell, K. W.; Liu, K.; Azadian, M.; Brunel, L. G.; Huang, Z.; Tran, H.; George, P. M.; Bao, Z. Conducting Polymer-Based Granular Hydrogels for Injectable 3D Cell Scaffolds. *Adv. Mater. Technol.* **2021**, *6* (6), 2100162.

For Table of Contents Only: